New Insights in the Bubble Wall of NGC 3324: Intertwined Substructures and a Bipolar Morphology Uncovered by JWST

L. K. Dewangan[1] , A. K. Maity[1,2] , Y. D. Mayya[3] , N. K. Bhadari[1,2] , Suman Bhattacharyya[4] , Saurabh Sharma[5] , and Gourav Banerjee[4]

[1] Astronomy and Astrophysics Division, Physical Research Laboratory, Navrangpura, Ahmedabad 380009, India; lokeshd@prl.res.in
[2] Indian Institute of Technology Gandhinagar Palaj, Gandhinagar 382355, India
[3] Instituto Nacional de Astrofísica, Óptica y Electrónica, Luis Enrique Erro # 1, Tonantzintla, Puebla, C.P. 72840, México
[4] Department of Physics and Electronics, CHRIST (Deemed to be University), Hosur Main Road, Bangalore, 560029, India
[5] Aryabhatta Research Institute of Observational Sciences, Manora Peak, Nainital 263002, India

Abstract

We report the discovery of intertwined/entangled substructures toward the bubble wall of NGC 3324 below a physical scale of 4500 au, which is the sharp edge/ionization front/elongated structure traced at the interface between the H II region and the molecular cloud. The sharp edge appears wavy in the Spitzer 3.6–8.0 μm images (resolution ~2″). Star formation signatures have mostly been traced on one side of the ionization front, which lies on the molecular cloud's boundary. The James Webb Space Telescope's (JWST) near- and mid-infrared images (resolution ~0″.07—0″.7) are employed to resolve the sharp edge, which has a curvature facing the exciting O-type stars. The elongated structures are associated with the 3.3 μm polycyclic aromatic hydrocarbon (PAH) emission, the 4.05 μm ionized emission, and the 4.693 μm H_2 emission. However, the PAH-emitting structures are depicted between the other two. The H_2 emission reveals numerous intertwined substructures that are not prominently traced in the 3.3 μm PAH emission. The separation between two substructures in the H_2 emission is ~1″.1 or 2420 au. The intertwined substructures are traced in the spatial areas associated with the neutral to H_2 transition zone, suggesting the origin of these structures by "thin-shell" instability. Furthermore, an arc-like feature traced in the Spitzer 3.6–8.0 μm images is investigated as a bipolar H II region (extent ~0.35 pc) at T_d ~25–28 K using the JWST images. A massive-star candidate VPHAS-OB1 #03518 seems to be responsible for the bipolar H II region.

Unified Astronomy Thesaurus concepts: Interstellar dust extinction (837); H II regions (694); Interstellar medium (847); Interstellar clouds (834); Star formation (1569); Pre-main sequence stars (1290)

1. Introduction

The space-based infrared and submillimeter observations obtained with the Spitzer and Herschel facilities have revealed bubbles (e.g., Churchwell et al. 2006, 2007) and filaments (e.g., André et al. 2010, 2014; Motte et al. 2018) as the major structures in star-forming regions. Several previous studies favor the involvement of these structures in the ongoing physical processes of star formation (e.g., Deharveng et al. 2010; Kumar et al. 2020). Such observed structures are extensively examined to study the origin of massive OB stars ($M_* \gtrsim 8\ M_\odot$) and their feedback processes, which are open research topics in the study of star formation (e.g., Zinnecker & Yorke 2007; Tan et al. 2014; Motte et al. 2018; Rosen et al. 2020). Now, the availability of high-resolution and high-sensitivity data from James Webb Space Telescope (JWST) provides us a unique opportunity to obtain more insights into physical processes operating in massive star-forming regions (e.g., Pontoppidan et al. 2022). One of the science cases of JWST[6] is to study the anatomy of photodissociation regions (PDRs) surrounding the H II regions. The JWST images, combined with the submillimeter and radio data sets, can be utilized to probe the molecular zone, the dissociation front, the

ionization front, the compressed structure, and the fully ionized flow of gas toward the edge of a H II region (see Berné et al. 2022). In this work, we have revisited the publicly available JWST near-infrared (NIR) and mid-infrared (MIR) images toward the boundary or bubble wall of the nearby young, star-forming region NGC 3324 (also known as "Cosmic Cliffs"; e.g., Pitts et al. 2019; Reiter et al. 2022). These JWST data are part of the public outreach products obtained through the JWST Early Release Observations (EROs).

1.1. Cosmic Cliffs, NGC 3324

Situated at a distance of 2.2 kpc (Göppl & Preibisch 2022; Pontoppidan et al. 2022; Reiter et al. 2022), NGC 3324 has a bubble-like appearance (e.g., Smith et al. 2010; Duronea et al. 2015; Reiter et al. 2022). Two O-type stars, HD 92206 and CPD −57°3580 (see Reiter et al. 2022, and references therein), have been reported as the major ionizing sources of NGC 3324 (see Figure A1(a) in the Appendix). The selected site in this work (i.e., the bubble rim or NGC 3324 field; see boxes in Figure A1(a)) is a part of NGC 3324, where pillar-like structures have been reported (see Figure 1(c) in Reiter et al. 2022). The bubble rim in NGC 3324 has the sharpest ionization boundary/front (see Smith et al. 2010; Duronea et al. 2015; Pontoppidan et al. 2022). Using various observational data sets, several studies have been performed toward NGC 3324 (e.g., Smith et al. 2010; Ohlendorf et al. 2013; Preibisch et al. 2014; Duronea et al. 2015; Zeidler et al. 2016; Pitts et al. 2019). Most recently, using the JWST infrared data, Reiter et al. (2022)

---

[6] https://webbtelescope.org

Table 1
List of Observational Surveys or Data Sets Utilized in This Work

Survey/Facility	Wavelength	Resolution (arcsec)	Reference
Sydney University Molonglo Sky Survey (SUMSS) at 843 MHz	35.56 cm	$\sim$45	Bock et al. (1999)
The Galactic Census of High and Medium-mass Protostars (CHaMP) ^{13}CO ($J = 1$–0) Survey	2.72 mm	$\sim$37	Barnes et al. (2011), Barnes et al. (2018)
Herschel Infrared Galactic Plane Survey (Hi-GAL)	70, 160, 250, 350, 500 μm	$\sim$5.8–37.0	Molinari et al. (2010a)
JWST ERO MIRI F770W, F1130W, F1280W, F1800W imaging facility	7.7, 11.3, 12.8, 18 μm	$\sim$0.44–0.70	Rieke et al. (2015), Wright et al. (2015)
Spitzer Galactic Legacy Infrared Mid-Plane Survey Extraordinaire (GLIMPSE)	3.6, 4.5, 5.8, 8.0 μm	$\sim$2	Benjamin et al. (2003), GLIMPSE Team (2020)
JWST ERO NIRCam Long Wavelength (LW) F335M, F444W, F470N imaging facility	3.365, 4.421, 4.707 μm	$\sim$0.17	Rieke et al. (2005), Beichman et al. (2012)
JWST ERO NIRCam Short Wavelength (SW) F090W, F187N, F200W imaging facility	0.901, 1.874, 1.99	$\sim$0.07	Rieke et al. (2005), Beichman et al. (2012)
Hubble Space Telescope (HST) ACS/WFC F658N imaging facility	6563 μm+ 6583 μm	$\sim$0.067–0.156	Smith et al. (2010)

reported several outflows including molecular hydrogen objects and Herbig–Haro flows in the NGC 3324 field, and many of these outflows are traced near the ionization front (see their paper for more details). It is thought that star formation activity or the presence of a population of actively accreting young stars/young stellar objects (YSOs) in the NGC 3324 field has been affected by feedback from the O-type stars (e.g., Reiter et al. 2022).

Using the JWST Near-Infrared Camera (NIRCam; Rieke et al. 2005; Beichman et al. 2012) and Mid-Infrared Instrument (MIRI; Rieke et al. 2015; Wright et al. 2015) images (resolution $\sim$0$\farcs$07–0$\farcs$7), on a small physical scale ($\sim$4500 au), there has been no attempt made to examine the H$_2$ emission and the polycyclic aromatic hydrocarbon (PAH) emission toward the ionization front in NGC 3324. Additionally, there is no study reported to probe embedded structures (such as bubbles/shells, pillar-like features, and small-scale substructures) and their role in the ongoing physical processes in the direction of the NGC 3324 field. In this context, we employed ratio and continuum-subtracted maps created from the JWST images to study various emission components (i.e., molecular, atomic, and ionized emission) down to physical scale of 4500 au, allowing us to probe ongoing physical processes in the NGC 3324 field.

In Section 2, we deal with the observational data sets adopted in this paper. Our observational findings are presented in Section 3. In Section 4, we discuss the implications of our outcomes derived toward the NGC 3324 field. In Section 5, we provide the conclusions of the present work.

2. Data Sets

This paper uses several publicly available data sets at different wavelengths (see Table 1). A large-scale area studied in this paper has an extent of $\sim$8$\farcm$5 $\times$ 9$\farcm$8 (central coordinates: $\alpha_{2000} = 10^h36^m43\fs25$; $\delta_{2000} = -58°37'12\farcs82$; see the solid box in Figure A1(a)).

We used the Hubble Space Telescope (HST[7]) F658N image (Proposal ID: 10475; PI: Smith, Nathan) taken with the Wide-Field Channel (WFC) of the Advanced Camera for Surveys (ACS). In the direction of our target site, the level-3 science-ready JWST[8]ERO NIRCam and MIRI images (program ID #2731; PI: Pontoppidan) were downloaded from the MAST

archive. One can also find more details of JWST performance in Rigby et al. (2023). More details about these JWST data sets are given in Reiter et al. (2022).

The Herschel dust temperature map[9](resolution $\sim$12$''$) is explored in this work, which was produced for the EU-funded ViaLactea project (Molinari et al. 2010b) using the Herschel continuum images at 70–500 μm (Molinari et al. 2010a) and the Bayesian PPMAP procedure (Marsh et al. 2015, 2017).

3. Results

A large-scale view of NGC 3324 is presented in Figure A1(a) (see the Appendix). In Figures A1(a)–(d), the distribution of ionized emission, molecular gas, and YSOs is examined in the direction of NGC 3324.

3.1. Multiscale View of NGC 3324: Intertwined Substructures

Figure 1(a) presents the Spitzer 5.8 μm image of the bubble rim. The visual inspection of the Spitzer map displays the ionization front (or a sharp edge of the cavity within NGC 3324), and its footprint is also indicated by a dotted curve (in red) in Figure 1(a). The positions of the previously identified candidate driving sources for the H$_2$ outflows (from Reiter et al. 2022) and the YSOs (from Kuhn et al. 2021) are also marked in Figure 1(a) (see also the Appendix). The sharp edge has a filamentary appearance and appears wavy. Massive 870 μm dust continuum clumps ($>$200 $M_\odot$; Duronea et al. 2015) are distributed toward this elongated and sharp edge. The positions of these clumps are also shown by filled stars in Figure 1(a). From the edge-on view, it appears that we see the sharp or narrow boundary, but from the face-on view, it might just be a sheet.

A small region labeled "sm1" is indicated by a solid box in Figure 1(a), where an interesting arc-like feature with dust temperature (T_d) of $\sim$25–28 K is evident. The values of T_d are obtained from the examination of the publicly available Herschel dust temperature map (see the Appendix for more details).

Using the Spitzer 3.6 μm band ($\lambda_{eff}/\Delta\lambda$: 3.55/0.75 μm) and 4.5 μm band ($\lambda_{eff}/\Delta\lambda$: 4.49/1.0 μm) images, Figure 1(b) presents a ratio map of 4.5 μm/3.6 μm emission for the same area as presented in Figure 1(a). The ratio map allows us to separate the features of 4.5 and 3.6 μm emission as bright and
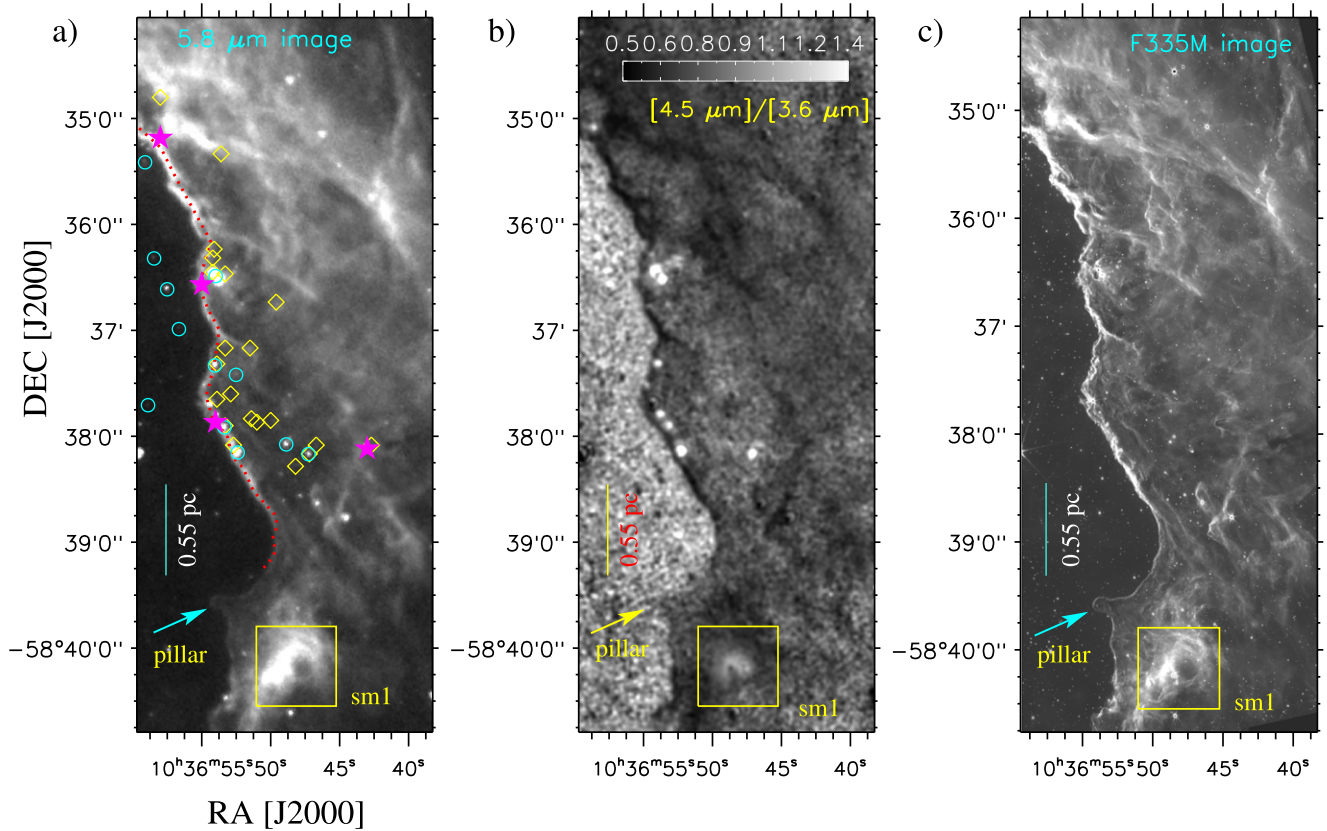
Figure 1. (a) The Spitzer-GLIMPSE 5.8 μm image of the bubble rim or NGC 3324 (see the dotted–dashed box in Figure A1(a)). The area of the image is $\sim 2'.79 \times 6'.74$ (central coordinates: $\alpha_{2000} = 10^h36^m49^s.02$; $\delta_{2000} = -58°\,37'25''.52$). The positions of four clumps traced in the LABOCA 870 μm continuum map (Duronea et al. 2015) are marked by filled stars. Open circles and open diamonds show the locations of YSOs (from Kuhn et al. 2021) and molecular outflows (from Reiter et al. 2022), respectively. A dotted curve (in red) shows the footprint of the sharp edge. (b) Spitzer-GLIMPSE ratio map of 4.5 μm/3.6 μm emission. (c) The JWST F335M image. In each panel, a small region "sm1" is highlighted by a solid box, and a scale bar shows a size of 0.55 pc at a distance of 2.2 kpc.

dark areas, respectively. One can find more details about this ratio map in Dewangan et al. (2016b, 2017). A prominent molecular hydrogen line emission ($\nu = 0$–0 $S(9)$; 4.693 μm) and a hydrogen recombination line Brα (4.05 μm) are covered by the Spitzer 4.5 μm band. The Spitzer 3.6 μm band encompasses a strong PAH emission at 3.3 μm, which originates from the PDRs. The sharp edge or the sharp ionization front is found with the excess 3.6 μm emission (see dark-gray/black areas). Several bright areas having the excess 4.5 μm emission are detected close to the ionization front, where noticeable YSOs and dust clumps are distributed (see Figure 1(a)). In the direction of the arc-like feature (see the small region "sm1" in Figure 1(a)), the excess 4.5 μm emission (see bright areas) is traced.

In Figure 1(c), we have examined the sharp edge of the cavity within NGC 3324 using the NIRCam image (at JWST F335M). One can compare different wavelength images of the sharp edge in Figure 1. In particular, the JWST F335M image is used to probe substructures of the features seen in the Spitzer image (see the sharp edge and the region "sm1"). One can also find noticeable substructures toward wavy structures as appeared in Figures 1(a) and (b).

The JWST NIRCam and MIRI images are presented in Figure 2. One can note that the coverage of NIRCam and MIRI instruments was taken into consideration while choosing the area shown in Figure 2, which does not cover the area containing the small region "sm1" as presented in Figure 1. Figure 2(a) displays a three-color composite map derived using

the JWST F470N (in red), F444W (in green), and F335W (in blue) images. The F470N − F444W image has been used to trace the 4.693 μm continuum-subtracted H$_2$ emission (e.g., Reiter et al. 2022). Hence, noticeable outflow signatures depicted in the narrowband F470N ($\lambda_{eff}/\Delta\lambda$: 4.707/0.051 μm) image are clearly evident as red color features in Figure 2(a), which have been thoroughly discussed in Reiter et al. (2022). The JWST NIRCam images (including the F470N − F444W image) reveal the presence of two substructures toward the sharp edge of the cavity within NGC 3324, which also seem to overlap each other at many places. Hence, such a configuration indicates the presence of intertwined substructures or double helical-like structures (see arrows in Figure 2(a)).

In Figure 2(b), we display a three-color composite map produced using the F1800W (in red), F1130W (in green), and F770W (in blue) images. The locations of previously reported YSOs and candidate driving sources for the H$_2$ outflows are also presented in Figure 2(b). The intertwined configuration is also evident in the JWST MIRI images as seen in the JWST NIRCam images. In order to further examine the intertwined substructures, we processed the JWST F1800 image with an edge detection algorithm (i.e., "Edge-DoG" filter), which uses the technique of difference of Gaussians filters (e.g., Assirati et al. 2014). The inset of Figure 2(b) is a two-color composite map produced using the "Edge-DoG"-processed JWST F1800 image (in red) and the JWST F1800 image (in turquoise), clearly showing the twisting/coupling of substructures (or intertwined substructures). Although this color composite map
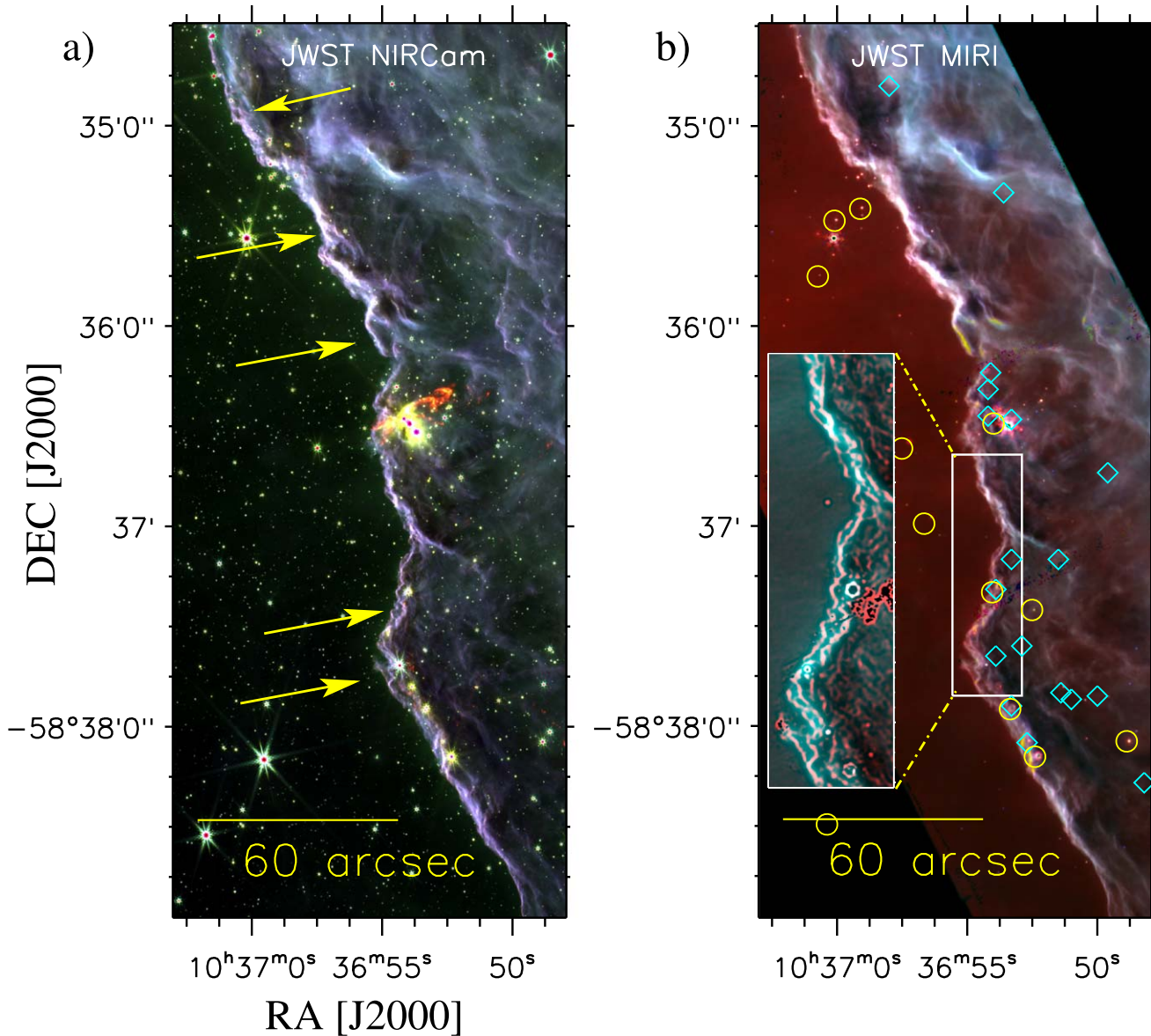
Figure 2. (a) A three-color composite map produced using the JWST F470N (in red), F444W (in green), and F335W (in blue) images (see the dotted box in Figure A1(a)). Arrows highlight elongated substructures. (b) A three-color composite map made using the F1800W (in red), F1130W (in green), and F770W (in blue) images. Circles and diamonds show the locations of YSOs and molecular outflows, respectively (see Figure 1(a)). An inset on the lower left presents the region in zoomed-in view (see the solid box in Figure 2(b)). The inset is a two-color composite map produced using the "Edge-DoG"-processed JWST F1800 image (in red) and the JWST F1800 image (in turquoise). In each panel, a scale bar shows a size of 60″ (or 0.64 pc at a distance of 2.2 kpc).

is produced for a small area as highlighted by the box in Figure 2(b), similar features can be traced for the entire sharp edge of NGC 3324. This is a new finding, and its implication is discussed in Section 4.

3.2. Molecular, Neutral, and Ionized Emission toward Intertwined Substructures

Figure 3(a) displays the HST F658N image, which is compared with the JWST images (i.e., F444W and (F470N − F444W); see Figures 3(b) and (c)). The HST F658N filter transmits both Hα ($\lambda = 6563$ Å) and [N II] ($\lambda = 6583$ Å) emission (Smith et al. 2010). The resolution of the HST F658N image is equivalent to that of the JWST NIRCam SW images and is better than the spatial resolution of the JWST NIRCam LW images (see Table 1).

Interestingly, a noticeable elongated bright emission was seen toward the sharp ionization front in the HST F658N image. We have found that the elongated emission traced in the HST F658N image spatially matches with the location of the elongated radio continuum emission as detected in the SUMSS 843 MHz radio continuum map (see Figure A1(c) in the Appendix). Note that we do not find any substructures in the HST F658N image (see Figure 3(a)). The twisting of substructures associated with the H$_2$ emission is presented in the inset of Figure 3(c), which is the JWST (F470N − F444W) image exposed to the "Edge-DoG" algorithm. In general, the H$_2$ molecules get excited by the UV/far-UV (FUV) photons or mechanical heating by shocks (i.e., from outflows, expanding H II regions, and stellar winds), which results in the FUV-fluorescence H$_2$ emission in a given star-forming region (e.g., Jo et al. 2017). We have examined the extent of the previously
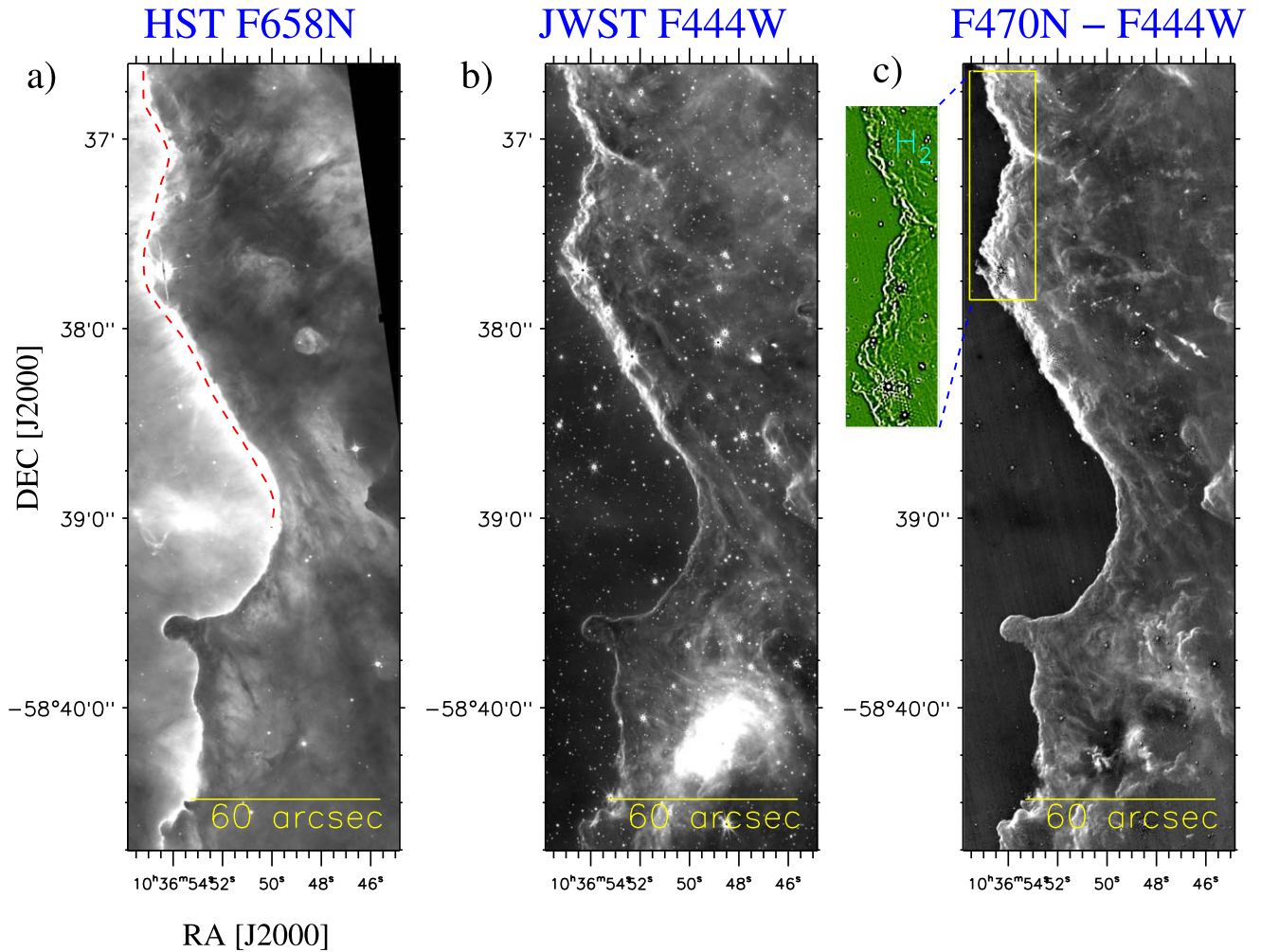
Figure 3. (a) HST F658N image. A dashed curve (in red) indicates the diffuse emission. (b) JWST F444W image. (c) F470N−F444W (in linear scale). An inset on the upper left shows the region in zoomed-in view (see the solid box in Figure 3(c)). The inset is the "Edge-DoG"-processed F470N−F444W image. In each panel, the scale bar corresponding to 60″ (or 0.64 pc at a distance of 2.2 kpc) is shown.

reported H_2 outflows (from Reiter et al. 2022) in the JWST (F470N − F444W) image (see Figure 3(c)), which do not match with our highlighted H_2 structures. Hence, the filamentary appearance of the H_2 emission is unlikely to be explained by outflow-driven shocks. Therefore, the H_2 emission associated with the substructures seems to be excited by the UV/FUV heating by ionizing sources of NGC 3324.

The NIRCam F187N, NIRCam F444W, MIRI F1280W, and MIRI F1800W filters contain the 1.87 μm Paα hydrogen recombination line, the 4.05 μm Brα hydrogen recombination line, the 12.81 μm [Ne II] line, and the 18.7 μm [S III] line, respectively, enabling us to trace the ionized emission. The NIRCam F335M, MIRI F770W, and MIRI F1130W bands cover the 3.3, 7.7, and 11.3 μm PAH features, respectively (Tielens 2008). Using the JWST NIRCam F444W ($\lambda_{eff}/\Delta\lambda$: 4.421/1.024 μm) and F335M ($\lambda_{eff}/\Delta\lambda$: 3.365/0.347 μm) images, we have produced the ratio map of F444W/F335M, which may allow us to probe the 3.3 μm PAH feature (via dark-gray/black areas). It is supported with the fact that the JWST NIRCam F444W filter does not contain the 3.3 μm PAH feature. Bright areas in this JWST ratio map show regions with the prominent 4.05 μm Brα feature and/or the 4.693 μm H_2 emission (see also the interpretation of the Spitzer ratio map in Section 3.1). We can readily locate the regions with the 4.05

μm Brα emission in the JWST ratio map by taking into account the areas with the 4.693 μm H_2 emission detected in the JWST F470N − F444W image.

We present Figure 4 to trace different emission components toward the sharp ionization front. Figure 4(a) shows a two-color composite map, which is the same as presented in the inset of Figure 2(b). In Figure 4(b), we display the JWST (F470N − F444W) image, which is exposed to the "Edge-DoG" algorithm (Figure 3(c)). Figure 4(c) presents the "Edge-DoG"-processed F444W/F335M image, enabling us to depict the PAH emission (dark areas) and the 4.05 μm Brα emission (bright areas). Figures 4(a) and (b) are shown here only for comparison purposes. The intertwined configuration is not very clearly seen in the "Edge-DoG"-processed F444W/F335M image, which also seems to reveal the PAH (or neutral) emission and the Brα (or ionized) emission to be in close proximity to each other.

In Figure 4(d), we produce a three-color composite map ("Edge-DoG"-processed F470N−F444W image (in red), "Edge-DoG"-processed F444W/F335M image (in green), and HST F658N image (in blue)). In these two "Edge-DoG"-processed images, to examine the spatial locations of the PAH and H_2 emission, emission/brightness profiles (not shown here) are also produced along a solid line (in yellow) marked in
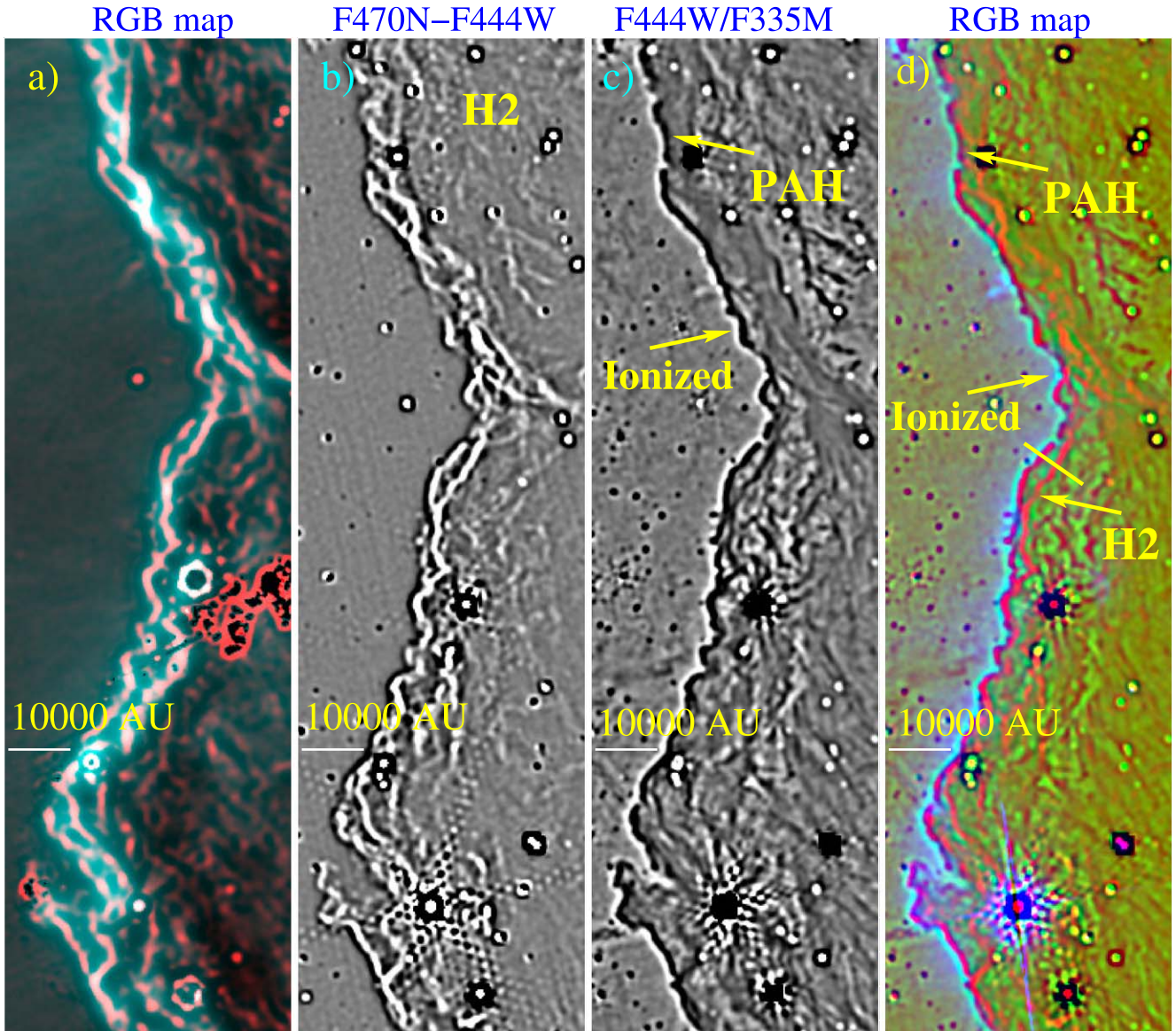
Figure 4. (a) Same as the inset shown in Figure 2(b). (b) Same as the inset shown in Figure 3(c). (c) The "Edge-DoG"-processed F444W/F335M image (see the solid box in Figure 2(b)). (d) A three-color composite map ("Edge-DoG"-processed F470N−F444W image (in red), the "Edge-DoG"-processed F444W/F335M image (in green), and the HST F658N image (in blue).

Figure 4(d). The HST F658N bright emission spatially coincides with the 4.05 μm Brα emission. The true boundary of the PDR is traced by H_2 emission and PAH emission, where the UV light is absorbed. More details of these outcomes are discussed in Section 4.

3.3. Discovery of a Bipolar Morphology in the Region "sm1"

In the direction of the region "sm1," the JWST images at different wavelengths are presented in Figures 5(a)–(e), respectively. As highlighted earlier (see Figure 1(a)), the Spitzer and Herschel images of "sm1" reveal an arc-like feature with the excess 4.5 μm emission and the warm dust emission ($T_d \sim$ 25–28 K; see Figure A1). Using the JWST NIRCam and MIRI images, Figure 5(f) displays a three-color composite map (F1130W (in red), F770W (in green), and F335W (in blue) images) to examine the locations of the PAH emission. Note that the entire selected area of "sm1" is not covered by the JWST MIRI images. Figures 5(g) and (h) show the F470N

−F444W and F444W/F335M images, respectively. In Figure 5(i), a two-color composite map (F444W/F335M (in red) and F470N−F444W (in turquoise) images) is presented, where the position of an OB star candidate (UCAC4 157-048728 or VPHAS-OB1 #03518; from Mohr-Smith et al. 2017) is also indicated by an arrow (see also Figures 5(c) and (d)).

The presence of H_2 emission is depicted in the F470N −F444W image (see Figure 5(g)). On the basis of a visual assessment, at least three H_2 depression regions (i.e., CC-1, CC-2, and CC-3) are identified in Figure 5(g) and are surrounded by the H_2 emission. Additionally, we have also marked one prominent structure in the JWST NIRCam images (see the dashed circle in panels of Figure 5), which is found with the intense H_2 emission (see also Figure 5(g)). In particular, the region CC-1 is very prominently seen in the longer-wavelength images (>2 μm), appearing like a bubble feature. The distance of the massive-star candidate UCAC4
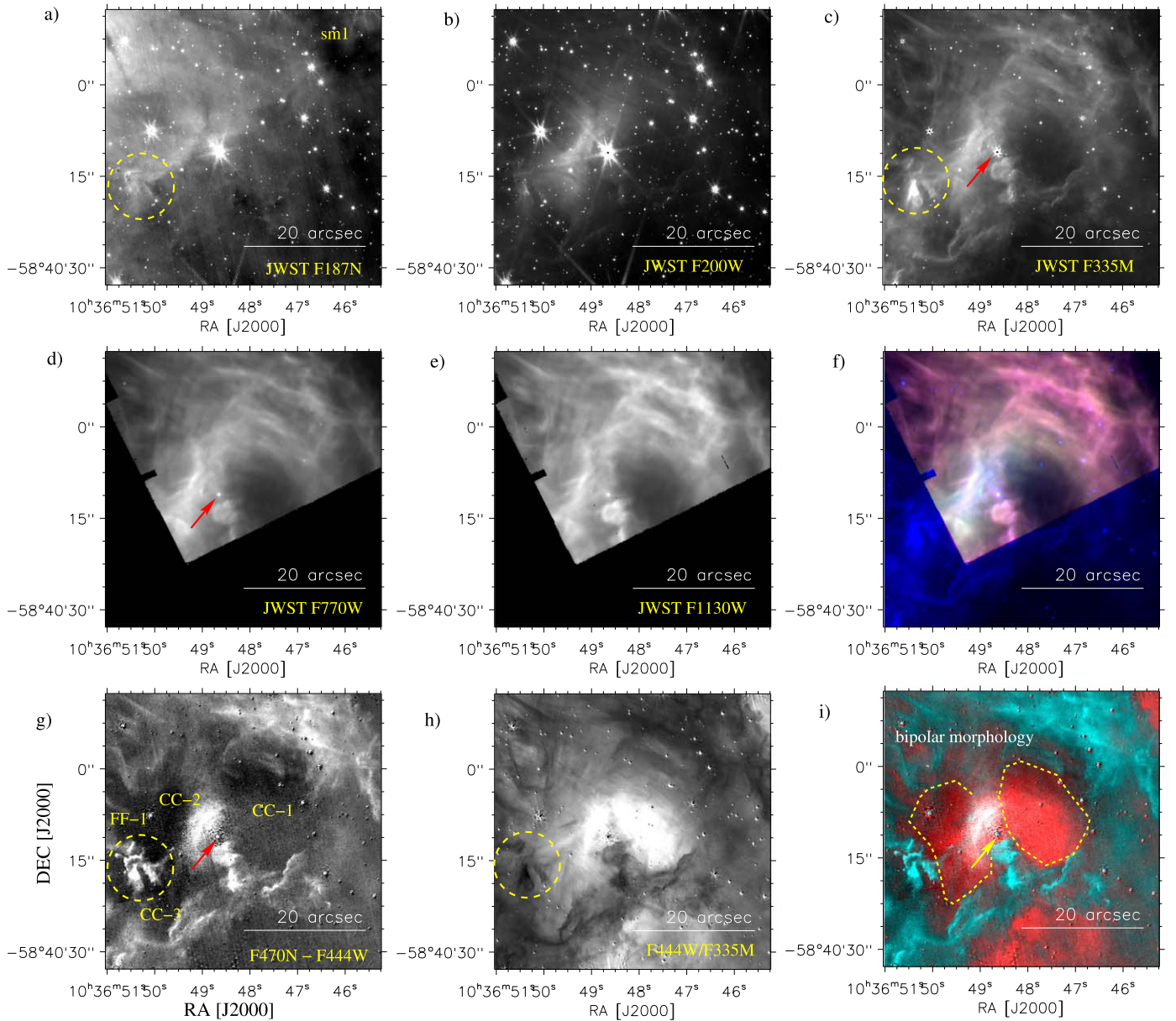
Figure 5. Multiwavelength view of an area "sm1" as indicated by the solid box in Figure 1(a). (a–e) JWST images at F187N, F200W, F335M, F770W, and F1130W are displayed, respectively. (f) A three-color composite map (F1130W (in red), F770W (in green), and F335W (in blue) images in linear scale). (g) F470N−F444W (in linear scale). (h) F444W/F335M (in linear scale). (i) A two-color composite map (F444W/F335M (red) and F470N−F444W (turquoise) images in linear scale). In panels (c), (d), and (g), an arrow shows the position of an OB star candidate (UCAC4 157-048728 or VPHAS-OB1 #03518; Mohr-Smith et al. 2017). In panel (g), three H$_2$ depression regions (i.e., CC-1, CC-2, and CC-3) and one emission structure (FF-1) are labeled. In panel (i), a bipolar morphology is highlighted, and the position of the OB star candidate UCAC4 157-048728 is found at its waist. In each panel, a scale bar corresponding to 20″ (or 0.21 pc at a distance of 2.2 kpc) is drawn.

157-048728 or VPHAS-OB1 #03518 toward "sm1" is about 2.3 pc (Bailer-Jones et al. 2018), suggesting its association with our target region. The position of UCAC4 157-048728 is not seen at the center of any H$_2$ depression regions (see the arrow in Figure 5(g)). Based on the published results of the Spitzer MIR bubbles hosting H II regions, the exciting source or massive star is anticipated to be located near the center of the bubbles (e.g., Churchwell et al. 2006, 2007; Deharveng et al. 2010). Hence, considering the locations of CC-2, CC-3, and the candidate massive star, we avoid proposing CC-1 as a bubble. In the direction of our selected area "sm1," we do not find any locations of the molecular outflows (see diamonds in Figure 1(a)). Hence, the observed H$_2$ emission in Figure 5(g)

is unlikely to be produced from shocks originating via outflows.

In Figure 5(h), the F444W/F335M image enables us to trace regions displaying the excess 4.44 μm emission (see bright areas) and/or 3.35 μm emission (see dark-gray/black areas). In other words, extended bright areas may show the Brα emission at 4.05 μm or the ionized emission due to the excess 4.44 μm emission, while dark-gray/black areas may display the PAH emission at 3.3 μm due to the excess 3.35 μm emission. The H$_2$ emission is detected toward the areas having the excess 3.35 μm emission (see Figures 5(g) and (h)). The extended ionized emission traced in the F444W/F335M image appears to be surrounded by the H$_2$ emission and the PAH emission (see
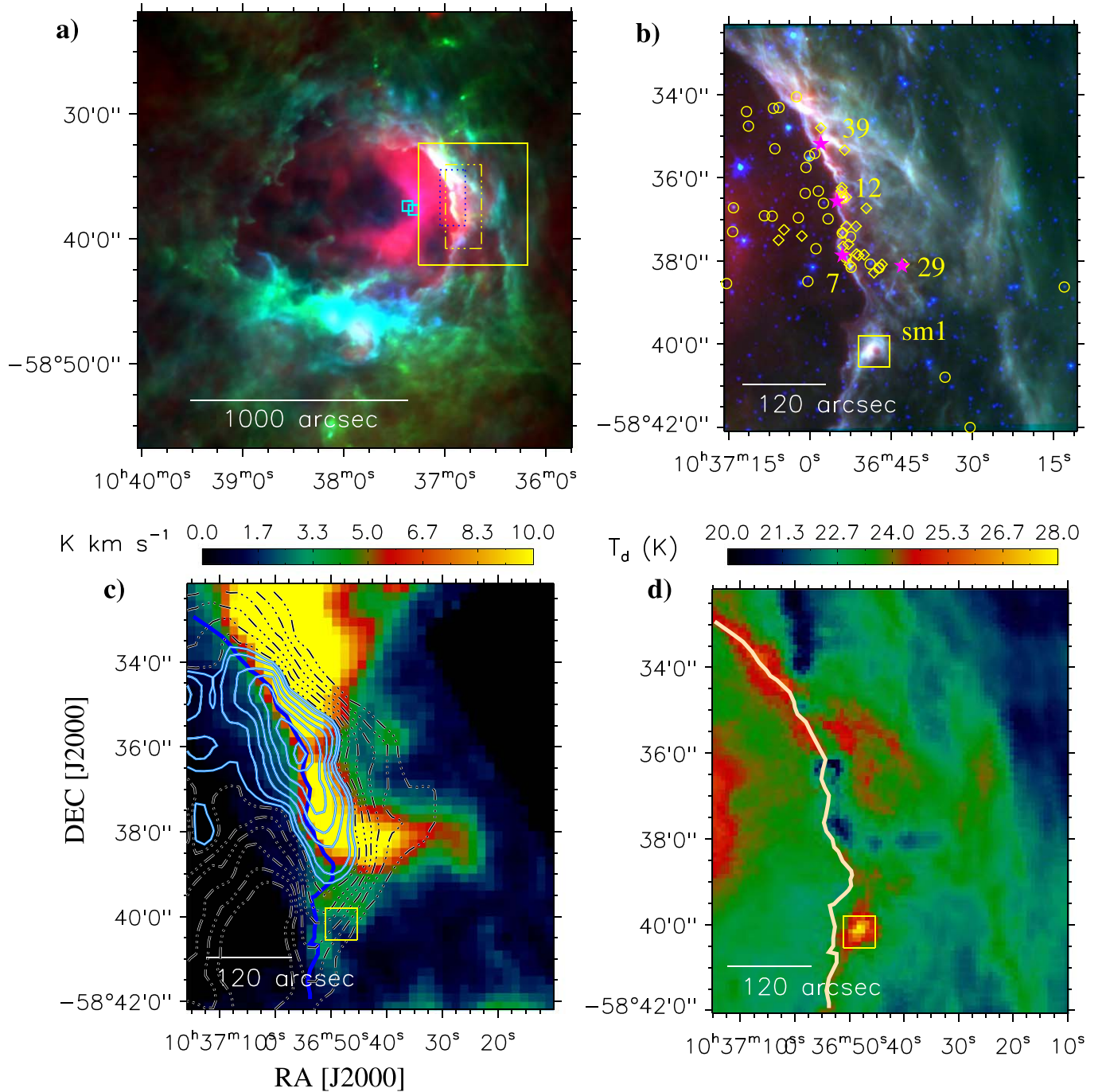
Figure A1. (a) Large-scale view of NGC 3324 using a three-color composite map (SUMSS 843 MHz (in red), Herschel 160 μm (in green), and Herschel 70 μm (in blue) images). Squares show the locations of massive O-type stars. Boxes indicate areas that are examined in this work. A solid box encompasses an area presented in Figures A1(b), (c), and (d). (b) A three-color composite map (Herschel 70 μm (in red), Spitzer 8.0 μm (in green), and Spitzer 3.6 μm (in blue) images in linear scale). The area of the image is $\sim$8$'$.5 $\times$ 9$'$.8 (central coordinates: $\alpha_{2000} = 10^h36^m43^s.25$; $\delta_{2000} = -58\,^\circ\,37'12''.82$). All the symbols are the same as presented in Figure 1(a). The dust continuum clumps highlighted by stars are also labeled. (c) Overlay of the SUMSS 843 MHz radio continuum contours on the CHaMP ^{13}CO moment-0 map at $[-24.3, -19.9]$ km s^{-1}. The SUMSS 843 MHz radio continuum contours (see dotted–dashed contours) are plotted with the levels of 46.5, 62.3, 78, 94, 109, and 125 mJy beam^{-1}. The SUMSS contours (see solid contours) are presented with the levels of 132, 141, 157, 172, 188, 204, and 212 mJy beam^{-1}. (d) Herschel dust temperature map. In panels (c) and (d), a thick curve shows the footprint of the sharp edge as seen in Figure A1(b). In panels (b), (c), and (d), a small region (i.e., "sm1") is indicated by a small yellow box. Scale bars are shown (at 1000$''$ (or 10.7 pc at a distance of 2.2 kpc) and 120$''$ (or 1.28 pc)).

Figure 5(i)). All the selected H$_2$ depression regions (i.e., CC-1, CC-2, and CC-3) seem to be filled with the ionized emission.

Figure 5(i) supports the existence of a bipolar H II region or a bipolar morphology (extent $\sim$0.35 pc), and the OB star candidate appears to be located at the central part of the waist of this bipolar morphology (see dashed curves in Figure 5(i)),

where we have detected noticeable PAH and H$_2$ emissions. In known bipolar H II regions (see Deharveng et al. 2010), the location of the exciting source(s) is expected toward the waist of the bipolar structures (e.g., IRAS 17599−2148, Dewangan et al. 2012, 2016c; W42, Dewangan et al. 2015). The structure FF-1 associated with the PAH and H$_2$ emissions appears to be

located at the edge of the bipolar morphology. Locally, the impact of the massive star (UCAC4 157-048728) or UV-fluorescence emission appears to be the cause of the H$_2$ emission (see the observed morphology in Figures 5(g) and (i)). More discussions on these observed results are presented in Section 4.2.

4. Discussion

4.1. Origin of Intertwined Substructures in PDRs

In general, the study of the H II regions powered by massive OB stars can allow us to explore the transitional boundary between the neutral/molecular PDR and the fully ionized H II region, where temperature and density differences across the boundary can cause evaporative flows and fluid dynamical instabilities (e.g., Hartigan et al. 2012; Goicoechea et al. 2016). Goicoechea et al. (2016) presented a diagram concerning the structure of a strongly UV-irradiated molecular cloud edge, where the ionization front, dissociation front, and compressed structure are outlined in the PDR near a H II region. The PDR initiates at the border of a H II region and extends up to the edge of the cold molecular cloud. This predominantly includes neutral and ionized species, resulting from chemical reactions induced by the FUV radiation emitted by the OB stars (Goicoechea et al. 2016). In PDRs, the H$_2$ emission peaks farther away from the ionizing star and is originated by the UV/FUV radiation or shock heating processes at the shock/dissociation front. Furthermore, the Brγ (or Brα) and Hα emission may trace photoevaporative flows from the PDRs (e.g., Carlsten & Hartigan 2018; Wolfire et al. 2022). Therefore, in general, the different flows (or gas layers) with varying temperatures and densities in the PDR can induce instabilities and give rise to the formation of complex structures. The high-resolution JWST images can be employed to directly observe the intricate interfaces of various emissions within the PDR.

The most prominent structure in the bubble wall of NGC 3324 is the sharp edge or the ionization front, which has a curvature that faces the locations of the previously reported O-type stars (i.e., HD 92206 and CPD $-57°3580$). The observed sharp edge is exposed to the harshest feedback from the powering O-type stars (e.g., Reiter et al. 2022). Using the JWST NIRCam and MIRI images, the presence of two coupled (or intertwined) substructures, below a physical scale of 4500 au, is investigated toward the sharp ionization front (see Figures 3(c) and 4(b)). The elongated structure seen in the 3.3 μm PAH emission is traced between the ionized emission and the 4.693 μm H$_2$ emission. The HST F658N bright emission spatially coincides with the 4.05 μm Brα emission. In Figure 4(d), an offset ($\sim0\farcs4$–$1\farcs1$ or 880–2420 au) is evident between the ionized emission and the FUV-fluorescence H$_2$ emission (see also Section 3.2). The twisting of substructures associated with the H$_2$ emission is depicted; however, such a configuration is not clearly traced in the PAH emission toward the higher decl. (or northern areas). Based on the intensity profile inspection, the separation between two substructures in the H$_2$ emission is $\sim1\farcs1$ (or 2420 au; see the solid yellow line in Figure 4(d) and also Section 3.2). We do not find any previously reported molecular outflows and YSOs toward the elongated structure linked with the PAH emission (see Figure 2(b)). Interestingly, the spatial areas associated with

the neutral/PAH and H$_2$ emission in PDRs seem to be resolved in the JWST images (see Figure 4(d)).

According to Kirsanova et al. (2023), the separation between the ionization and dissociation fronts in the S255 H II region (d ~2.06 kpc) and the S257 H II region (d ~2.5 kpc) is determined to be about 0.3–0.4 pc. In this relation, they used the 2.16 μm Brγ and the 2.12 μm H$_2$ line emission. Based on this observational information, they evaluated the applicability of models of a uniform medium and a nonuniform (clumpy) structure of the PDRs. They suggested that the derived value of ~0.3–0.4 pc is consistent with a clumpy medium and should be 10–20 times lower (i.e., ~3000 au (or 0.015 pc) to 8000 au (or 0.04 pc)) in a uniform gas density. In our selected target, the H$_2$ dissociation front and the H ionization front (or PAH) are not merged. The transition from PAH to H$_2$ is abrupt with sharp edges and with the offset value of ~2420 au (see Figure 4(d)). Taking into account these observational findings, numerical simulations of uniform/nonuniform gas density may be carried out to obtain more insights in the bubble wall of NGC 3324. Such an exercise, however, is beyond the scope of the current work.

It has been proposed that instabilities at the ionization front (or the dissociation front) can be responsible for the irregular shapes of observed H II regions, including the "fingers" and "elephant trunks" (Giuliani 1979; Garcia-Segura & Franco 1996; Williams 1999). Depending on how thick (Williams 2002) or thin (Giuliani 1979; Garcia-Segura & Franco 1996) the shell of shocked neutral gas is around the ionization front, the onset of different kinds of instability can be inferred (e.g., Henney 2007).

Following the work of Goicoechea et al. (2016), it is possible that the force imbalance between thermal (isotropic) and ram pressure (parallel to the flow) is what causes the instability known as the "thin shell" (see also Garcia-Segura & Franco 1996; Williams 2003). One can also expect entangled structures in astrophysical plasma on collisional (fluid) scales in the "thin-shell" instability (Dieckmann et al. 2015). Therefore, the intertwined/entangled substructures seem to be caused by the "thin-shell" instability. We further suggest that the intertwined/entangled substructures in the PDRs that have been discovered may be considered as one of the direct indicators of instability on the dissociation front. To further gain insights into the observed intertwined configuration, we will need new submillimeter dust continuum and molecular line data with a resolution comparable to the JWST images.

Signposts of star formation including massive stars (i.e., outflows, protostars, 6.7 GHz methanol masers, 22 GHz water masers, etc.) are often found at the edges of the Spitzer bubbles (e.g., Churchwell et al. 2006, 2007) that surround H II regions stimulated by massive OB-type stars (e.g., Deharveng et al. 2010; Dewangan et al. 2016b). Therefore, the JWST images will be very useful to probe ongoing star formation processes toward the edges of the bubbles.

4.2. Origin of the Bipolar Morphology Seen in the JWST Images

As mentioned earlier, a compact and arc-like feature in the small region "sm1" is identified using the Spitzer and Herschel images (see Section 3.3). Diffuse SUMSS 843 MHz radio continuum emission is present toward this selected region (see Figure A1). Due to the availability of high-resolution JWST images, apart from the sharp ionization front, we have also

Table 2
Pressure Components Driven by O9.5V and B0.5V Stars at $D_s = [0.5, 1]$ pc
(See Text for More Details)

Spectral Type of Star	N_{UV} (s^{-1})	P_{HII} at $D_s$at D_s (dynes cm^{-2})	P_{HII} at $D_s$at D_s (dynes cm^{-2})
O9.5V	1.2×10^{48}	7.5×10^{-10}	2.6×10^{-10}
B0.5V	6.3×10^{46}	1.7×10^{-10}	6.1×10^{-11}

Note. The values of N_{UV} for both the O9.5V and B0.5V stars are also listed.

examined this arc-like feature in this paper. In the direction of the arc-like feature, a bipolar morphology (extent ~0.35 pc) in "sm1" is investigated using the JWST images and is filled with the ionized emission (see Section 3.3). The massive-star candidate VPHAS-OB1 #03518 is found at the waist of the bipolar morphology. In order to infer the impact of VPHAS-OB1 #03518, we have determined three pressure components (i.e., pressure of a H II region (P_{HII}), radiation pressure (P_{rad}), and stellar wind ram pressure (P_{wind})) driven by the massive OB star following the approach by Dewangan et al. (2016b).

In the literature, we do not find the exact spectral class of this massive star. Therefore, the pressure calculations are performed separately for a B0.5V-type star and a star of O9.5V type. In general, in the case of massive zero-age main-sequence stars, the value of P_{HII} exceeds the values of P_{rad} and P_{wind} (e.g., Dewangan et al. 2016b). Note that Wolf–Rayet stars are an exception to this argument, where the P_{wind} value predominates over P_{HII} and P_{rad} values (e.g., Lamers & Cassinelli 1999; Dewangan et al. 2016a; Baug et al. 2019; Dewangan et al. 2022). Therefore, only the values of P_{HII} are computed in this paper at $D_s = [0.5, 1]$ pc. The values of D_s are higher than the extent of the bipolar morphology. Pressure components driven by O9.5V and B0.5V stars are determined and are tabulated in Table 2. Table 2 also lists the number of Lyman continuum photons emitted per second (N_{UV}) for both O9.5V and B0.5V stars (from Panagia 1973). The calculation uses the radiative recombination coefficient $\alpha_B = 2.6 \times 10^{-13}$ cm^3 s^{-1} at electron temperature T_e of 10^4 K. In the literature, pressure values (P_{MC}) for typical cool molecular clouds (particle density ~10^3–10^4 cm^{-3} and temperature ~20 K) have been reported to be ~2.8×10^{-12} dynes cm^{-2} to 2.8×10^{-11} dynes cm^{-2} (see Table 7.3 in Dyson & Williams 1997). Considering the values of P_{HII} (for both O9.5V and B0.5V stars) > P_{MC} (see Table 2), the impact of a massive OB star at a distance of [0.5, 1] pc seems to be possible.

Overall, in the selected region "sm1" of NGC 3324, the pressure measurements support the impact of the massive-star candidate VPHAS-OB1 #03518 on its surroundings, which is locally responsible for the bipolar morphology as seen in the JWST F470N−F444W and F444W/F335M images. High-resolution submillimeter observations and molecular line data with a resolution comparable to the JWST images will be helpful to further explore our proposed arguments in "sm1."

5. Summary and Conclusions

The current work employs a multiscale and multiwavelength approach in the direction of the bubble wall of NGC 3324 (d ~2.2 kpc) to examine ongoing physical processes. The present paper focuses on the sharp edge/elongated structure or the ionization front in NGC 3324, which is depicted at the interface between the H II region and the molecular cloud.

For the first time, using the JWST images at 0.9–18 μm, we have discovered intertwined/entangled substructures or a double helix toward the sharp ionization front below a physical scale of 4500 au. The JWST F470N−F444W image is utilized to study the H$_2$ emission at 4.693 μm, while the JWST F444W/F335M image has been employed to depict the PAH feature and the ionized emission. The elongated structure in the 3.3 μm PAH emission seems to be seen between the ionized emission and the H$_2$ emission. The presence of the ionized emission is inferred from the Brα (or Hα) emission. We find an offset (~$0\rlap{.}''4$–$1\rlap{.}''1$ or 880–2420 au) between the ionized emission and the UV-fluorescence H$_2$ emission.

The intertwined configuration is notably evident in the continuum-subtracted H$_2$ emission, which is less significant in the PAH emission at 3.3 μm. The two substructures in the H$_2$ emission are separated by at least ~$1\rlap{.}''1$ (or 2420 au). The presence of intertwined structures observed in JWST images toward the spatial regions linked to the neutral to H$_2$ transition zone suggest that these structures may have originated from the "thin-shell" instability.

Using the ionized, PAH, and H$_2$ emissions traced in the JWST images, we have also investigated a bipolar morphology or bipolar H II region (extent ~0.35 pc) at T_d ~25–28 K, which is away from the ionization front and is associated with the elongated molecular/dust cloud. A previously known massive OB star candidate (UCAC4 157-048728) is found at the waist of the bipolar morphology and seems to be locally responsible for it.

To further study the intertwined configuration, submillimeter dust continuum and molecular line data with a resolution comparable to the JWST images will be very useful. This study also indicates that intertwined substructures along the boundaries of the Spitzer bubbles hosting massive OB-type stars may be commonly detected characteristics that can be investigated with the JWST images.

Appendix
Multiwavelength View of NGC 3324

The morphology of NGC 3324 is presented in Figure A1(a), which is a three-color composite map (SUMSS 843 MHz (in red), Herschel 160 μm (in green), and Herschel 70 μm (in blue) images). The locations of massive O-type stars (i.e., HD 92206 and CPD $-57°3580$) are also marked by squares in Figure A1(a). The free–free emission tracing the ionized nebula in the SUMSS 843 MHz radio continuum map is distributed within the extended bubble NGC 3324. An area highlighted by the solid box in Figure A1(a) is presented in Figure A1(b), which shows a three-color composite map produced using the Herschel 70.0 μm far-infrared image (in red), Spitzer 8.0 μm MIR image (in green), and Spitzer 3.6 μm NIR image (in blue). In Figure A1(b), the positions of YSOs, 870 μm dust continuum clumps (at $d \sim 2.5$ kpc; IDs: 7 (mass $\sim530\ M_\odot$), 12 (mass $\sim390\ M_\odot$), 29 (mass $\sim390\ M_\odot$), and 39 (mass $\sim220\ M_\odot$); see Duronea et al. 2015, for more details), and molecular outflows are also highlighted by open circles, filled stars, and open diamonds, respectively. This paper is mainly focused on the sharp edge of the cavity within NGC 3324 (or the ionization front) and the arc-like feature toward the small region "sm1," which are evident in the Spitzer and Herschel images. Massive dust continuum clumps (mass range ~220–$530\ M_\odot$; Duronea et al. 2015) have been reported toward the sharp edge.

In the direction of NGC 3324, Figure A1(c) displays the integrated intensity (i.e., moment-0) map of CHaMP ^{13}CO $(J = 1-0)$ over a velocity range of $[-24.3,\ -19.9]$ km s^{-1}, revealing an elongated morphology. The moment-0 map is also overlaid with the SUMSS 843 MHz radio continuum contours. The radio continuum map favors the presence of an elongated feature (extent $\sim7\rlap{.}'5$) having an aspect ratio (i.e., length/width) of ~3, which seems to be located toward the sharp ionization front. Previously, Duronea et al. (2015) explored these two data sets toward NGC 3324. However, they did not discuss any elongated ionized feature. In the literature, we find that the energetic feedback from massive stars has been proposed to explain the existence of the elongated ionized features by swept-up ionized gas or dissipated turbulence (e.g., Emig et al. 2022). Hence, such ionized features are expected to be far from the exciting massive stars in the OB association/OB star complex (e.g., Karr & Martin 2003; Pon et al. 2014; Emig et al. 2022). Based on the spatial location of the elongated ionized feature with respect to the ionization front and the O-type stars, we suggest that the feedback from the massive O-type stars is likely the reason for the existence of the elongated ionized feature.

In Figure A1(d), we present the Herschel dust temperature map. Figures A1(c) and (d) cover the same area as displayed in Figure A1(b). The footprint of the ionization front is also marked by a solid curve in Figures A1(c) and (d). On the basis of Figures A1(c) and (d), we can study the spatial distribution of the molecular gas, dust temperature, and ionized emission with respect to the ionization front. At the molecular cloud's edge, the ionization front is seen, where variations of the dust temperature ($T_d \sim20$–28 K) are evident. Overall, the sharp edge appears to be situated at the molecular gas/H II region interface.

ORCID iDs

L. K. Dewangan https://orcid.org/0000-0001-6725-0483
A. K. Maity https://orcid.org/0000-0002-7367-9355
Y. D. Mayya https://orcid.org/0000-0002-4677-0516
N. K. Bhadari https://orcid.org/0000-0001-8812-8460
Suman Bhattacharyya https://orcid.org/0000-0002-1920-6055
Saurabh Sharma https://orcid.org/0000-0001-5731-3057
Gourav Banerjee https://orcid.org/0000-0001-8873-1171

References

André, P., Di Francesco, J., Ward-Thompson, D., et al. 2014, in Protostars and Planets VI, ed. H. Beuther et al. (Tucson, AZ: Univ. of Arizona Press), 27
André, P., Men'shchikov, A., Bontemps, S., et al. 2010, A&A, 518, L102
Assirati, L., Silva, N. R., Berton, L., Lopes, A. A., & Bruno, O. M. 2014, JPhCS, 490, 012020
Bailer-Jones, C. A. L., Rybizki, J., Fouesneau, M., Mantelet, G., & Andrae, R. 2018, AJ, 156, 58
Barnes, P. J., Hernandez, A. K., Muller, E., & Pitts, R. L. 2018, ApJ, 866, 19
Barnes, P. J., Yonekura, Y., Fukui, Y., et al. 2011, ApJS, 196, 12
Baug, T., de Grijs, R., Dewangan, L. K., et al. 2019, ApJ, 885, 68
Beichman, C. A., Rieke, M., Eisenstein, D., et al. 2012, Proc. SPIE, 8442, 84422N
Benjamin, R. A., Churchwell, E., Babler, B. L., et al. 2003, PASP, 115, 953
Berné, O., Habart, É., Peeters, E., et al. 2022, PASP, 134, 054301
Bock, D. C. J., Large, M. I., & Sadler, E. M. 1999, AJ, 117, 1578
Carlsten, S. G., & Hartigan, P. M. 2018, ApJ, 869, 77
Churchwell, E., Povich, M. S., Allen, D., et al. 2006, ApJ, 649, 759
Churchwell, E., Watson, D. F., Povich, M. S., et al. 2007, ApJ, 670, 428
Deharveng, L., Schuller, F., Anderson, L. D., et al. 2010, A&A, 523, A6
Dewangan, L. K., Baug, T., Ojha, D. K., et al. 2016a, ApJ, 826, 27
Dewangan, L. K., Luna, A., Ojha, D. K., et al. 2015, ApJ, 811, 79
Dewangan, L. K., Ojha, D. K., Anandarao, B. G., Ghosh, S. K., & Chakraborti, S. 2012, ApJ, 756, 151
Dewangan, L. K., Ojha, D. K., Luna, A., et al. 2016b, ApJ, 819, 66
Dewangan, L. K., Ojha, D. K., Zinchenko, I., et al. 2016c, ApJ, 833, 246
Dewangan, L. K., Ojha, D. K., Zinchenko, I., Janardhan, P., & Luna, A. 2017, ApJ, 834, 22
Dewangan, L. K., Pirogov, L. E., Bhadari, N. K., & Maity, A. K. 2022, MNRAS, 516, 2988
Dieckmann, M. E., Ahmed, H., Doria, D., et al. 2015, PhRvE, 92, 031101
Duronea, N. U., Vasquez, J., Gómez, L., et al. 2015, A&A, 582, A2
Dyson, J. E., & Williams, D. A. 1997, The Physics of the Interstellar Medium (Bristol: IOP Publishing)
Emig, K. L., White, G. J., Salas, P., et al. 2022, A&A, 664, A88
Garcia-Segura, G., & Franco, J. 1996, ApJ, 469, 171
Giuliani, J. L. J. 1979, ApJ, 233, 280
GLIMPSE Team 2020, GLIMPSE I Archive, IPAC doi:10.26131/IRSA210
Goicoechea, J. R., Pety, J., Cuadrado, S., et al. 2016, Natur, 537, 207
Göppl, C., & Preibisch, T. 2022, A&A, 660, A11
Hartigan, P., Palmer, J., & Cleeves, L. I. 2012, HEDP, 8, 313
Henney, W. J. 2007, in Diffuse Matter from Star Forming Regions to Active Galaxies - a Volume Honouring John Dyson, ed. S. A. E. G. Falle (Dordrecht: Springer), 103
Jo, Y.-S., Seon, K.-I., Min, K.-W., Edelstein, J., & Han, W. 2017, ApJS, 231, 21
Karr, J. L., & Martin, P. G. 2003, ApJ, 595, 880
Kirsanova, M. S., Tatarnikov, A. M., Boley, P. A., et al. 2023, AstBu, 78, 373
Kuhn, M. A., de Souza, R. S., Krone-Martins, A., et al. 2021, ApJS, 254, 33
Kumar, M. S. N., Palmeirim, P., Arzoumanian, D., & Inutsuka, S. I. 2020, A&A, 642, A87
Lamers, H. J. G. L. M., & Cassinelli, J. P. 1999, Introduction to Stellar Winds (Cambridge: Cambridge Univ. Press)
Marsh, K. A., Whitworth, A. P., & Lomax, O. 2015, MNRAS, 454, 4282
Marsh, K. A., Whitworth, A. P., Lomax, O., et al. 2017, MNRAS, 471, 2730
Mohr-Smith, M., Drew, J. E., Napiwotzki, R., et al. 2017, MNRAS, 465, 1807
Molinari, S., Swinyard, B., Bally, J., et al. 2010a, A&A, 518, L100
Molinari, S., Swinyard, B., Bally, J., et al. 2010b, PASP, 122, 314
Motte, F., Bontemps, S., & Louvet, F. 2018, ARA&A, 56, 41
Ohlendorf, H., Preibisch, T., Gaczkowski, B., et al. 2013, A&A, 552, A14
Panagia, N. 1973, AJ, 78, 929
Pitts, R. L., Barnes, P. J., & Varosi, F. 2019, MNRAS, 484, 305

Pon, A., Johnstone, D., Bally, J., & Heiles, C. 2014, MNRAS, 441, 1095
Pontoppidan, K. M., Barrientes, J., Blome, C., et al. 2022, ApJL, 936, L14
Preibisch, T., Zeidler, P., Ratzka, T., Roccatagliata, V., & Petr-Gotzens, M. G. 2014, A&A, 572, A116
Reiter, M., Morse, J. A., Smith, N., et al. 2022, MNRAS, 517, 5382
Rieke, G. H., Wright, G. S., Böker, T., et al. 2015, PASP, 127, 584
Rieke, M. J., Kelly, D., & Horner, S. 2005, Proc. SPIE, 5904, 1
Rigby, J., Perrin, M., McElwain, M., et al. 2023, PASP, 135, 048001
Rosen, A. L., Offner, S. S. R., Sadavoy, S. I., et al. 2020, SSRv, 216, 62
Smith, N., Bally, J., & Walborn, N. R. 2010, MNRAS, 405, 1153
Tan, J. C., Beltrán, M. T., Caselli, P., et al. 2014, in Protostars and Planets VI, ed. H. Beuther et al. (Tucson: Univ. of Arizona Press), 149

Tielens, A. G. G. M. 2008, ARA&A, 46, 289
Williams, R. J. R. 1999, MNRAS, 310, 789
Williams, R. J. R. 2002, MNRAS, 331, 693
Williams, R. J. R. 2003, in Revista Mexicana de Astronomía y Astrofísica, Winds, Bubbles, and Explosions: A Conference to Honor John Dyson 15 ed. S. J. Arthur & W. J. Henney, 184
Wolfire, M. G., Vallini, L., & Chevance, M. 2022, ARA&A, 60, 247
Wright, G. S., Wright, D., Goodson, G. B., et al. 2015, PASP, 127, 595
Zeidler, P., Preibisch, T., Ratzka, T., Roccatagliata, V., & Petr-Gotzens, M. G. 2016, A&A, 585, A49
Zinnecker, H., & Yorke, H. W. 2007, ARA&A, 45, 481